ACTA IMEKO
ISSN: 2221-870X
September 2026, Volume 15, Number 3, 1 - 16

Three-dimensional inertial measurement unit-based analysis of wheelchair racing propulsion using a Sensor-in-Glove System

Kimitomo Taniguchi[1], Tatsuru Ibusuki[2,4], Koichi Kawabata[3,4]

[1] *Department of Rehabilitation, Hiroshima International University, Hiroshima, Japan*
[2] *Rehabilitation Department, Akeno Central Hospital, Beppu, Oita, Japan*
[3] *Department of Rehabilitation, Takarazuka University of Medical and Health Care, Wakayama, Japan*
[4] *Department of Rehabilitation Medicine, Wakayama Medical University, Wakayama, Japan*

ABSTRACT
This study proposes the Sensor-in-Glove System (SIGS), a field-deployable method for measuring wheelchair racing propulsion during outdoor sprinting. SIGS synchronises two inertial measurement units (IMUs)—one embedded in a 3D-printed glove and one mounted on the wheel—to capture push cycle-wise hand and wheel kinematics. As a proof-of-concept validation, six elite athletes performed maximal-effort 100-m sprints. SIGS recorded continuous motion data, achieving a displacement-estimation error of 0.73 % over a 10-m interval. Propulsion onset and hand release were objectively identified from IMU signals without visual inspection, enabling the push cycle to be divided into mechanically meaningful phases. Newly defined 3D acceleration-vector metrics revealed individual push styles, and peak resultant acceleration showed strong correlations with wheelchair velocity (r = 0.82–0.95). Class-wise comparisons demonstrated significant differences in peak acceleration (F = 10.52, p < 0.001), indicating that SIGS captures impairment-specific push characteristics. As the first field-based 3D acceleration-vector analysis using a glove-embedded IMU, this study shows that SIGS provides a practical and quantitative approach for evaluating propulsion mechanics, and offers opportunities for technique assessment and athlete-specific performance analysis in wheelchair racing.

Section: RESEARCH PAPER

Keywords: wearable sensors; inertial measurement unit (IMU); wheelchair propulsion; three-dimensional acceleration analysis; para-athletics

Citation: K. Taniguchi, T. Ibusuki, K. Kawabata, Three-dimensional inertial measurement unit-based analysis of wheelchair racing propulsion using a Sensor-in-Glove System, Acta IMEKO, vol. 15 (2026) no. 3, pp. 1-16. DOI: 10.21014/actaimeko.v15i3.2353

Section Editor: Jakub Svatos, CVUT Prague, Czech Republic

Received March 26, 2026; **In final form** July 6, 2026; **Published** September 2026

Funding: This work was supported by the Wakayama Medical University Center for Future Medical Promotion (Grant 2023-03).

Corresponding author: Kimitomo Taniguchi, e-mail: taniguti@hirokoku-u.ac.jp

1. INTRODUCTION

Motion analysis is essential for advancing performance research in wheelchair racing, as it enables the examination of propulsion efficiency and mechanical characteristics. Previous studies have employed optical motion capture [1], [2], torque sensors [3], [4], inertial measurement unit [5], [6], and contact sensors [7]; however, these methods have all involved measurements conducted under various constraints [8]. Although the need for outdoor measurements, where variables such as rolling resistance and aerodynamics can be captured, has been highlighted to better reflect actual racing conditions, conventional approaches have not sufficiently addressed this requirement [8], [9]. Furthermore, a major limitation of traditional analyses is that the identification of hand contact (HC) and hand release (HR), the moments when the hand touches and leaves the handrim, relies on visually determining the instant the glove contacts the rim, which may introduce inter-rater variability [8], [10]–[12].

Despite substantial progress in wheelchair propulsion research, no existing method has enabled detailed, push-wise quantification of hand motion during outdoor sprinting. Optical motion-capture systems provide high spatial accuracy (< 2 mm) [13], but require controlled indoor environments and limited capture volumes, making them unsuitable for full-length sprint analysis. Torque-sensor-based wheels allow direct measurement of propulsion forces, but alter the athlete's habitual setup and are impractical for field use.

IMU-based approaches offer portability and have been used to estimate temporal variables or planar kinematics; however, no system has captured the three-dimensional motion of the hand itself, including the orientation of the acceleration vector during each push cycle. As a result, key aspects of propulsion—such as the precise timing of hand–rim contact and the direction in which force is applied—remain insufficiently understood in outdoor sprinting. A system capable of measuring 3D hand motion would provide new insight into how athletes generate and orient force, offering the potential for novel performance indicators beyond conventional temporal or torque-based metrics. A summary of representative measurement approaches used in previous wheelchair propulsion studies is provided in Table 1.

To address these limitations, we developed the Sensor-in-Glove System (SIGS), a glove-embedded IMU framework designed to capture push cycle-wise three-dimensional hand acceleration during outdoor wheelchair sprinting. In wheelchair racing, athletes propel their chairs using rigid gloves, and in recent years, these gloves have increasingly been produced using 3D printing. Leveraging this technological trend, we designed a glove with a dedicated space for embedding an IMU. Based on this concept, we developed SIGS, a novel measurement system that records hand motion using an IMU embedded in the glove, and simultaneously captures wheel rotation using another IMU mounted on the wheel. This configuration enables synchronised acquisition of hand kinematics and wheel dynamics, allowing the detection of subtle variations in push cycle timing and force application that are difficult to observe with conventional methods.

SIGS offers four major advantages. First, unlike optical systems, it does not require high-speed cameras or indoor environments, enabling immediate measurement in outdoor stadium settings. Second, SIGS allows data collection using the athlete's own racing gloves, eliminating the need for specialised laboratory equipment. Third, the system can record the entire 100-m sprint without restricting the measurement zone, allowing comprehensive analysis of propulsion under real-race conditions. Fourth, instead of relying on visual judgment of handrim contact, SIGS objectively and quantitatively identifies push events based on IMU signals, thereby improving reproducibility. These advantages suggest that SIGS has strong potential as a practical and scalable tool for field-based performance assessment.

In this study, we report measurements obtained using SIGS during maximal-effort 100-m sprints performed on an outdoor track by six athletes classified under World Para Athletics categories T52, T53, and T54 (two athletes per class). Using the acceleration recorded by the glove-mounted IMU during push, we calculated the magnitude and direction of the applied forces and examined push characteristics across participants. The analysis of the magnitude and direction of these acceleration vectors revealed pronounced differences in the direction of force application among participants, as well as distinct characteristics across propulsion sections, such as immediately after the start and near the finish. Furthermore, individual variability was also observed in the magnitude, azimuth, and elevation of the acceleration vector at the moment of peak resultant acceleration within each push cycle, suggesting that even within the same impairment classification, athletes employ different force-orientation patterns and push strategies. Given the limited sample size, this study is positioned as a preliminary investigation demonstrating the novelty and feasibility of the proposed measurement method. This study was approved by the Life Sciences and Medical Research Ethics Committee of Hiroshima International University (approval no.: 23-009).

2. METHODS

2.1. Participants

Six wheelchair racing athletes, with experience competing in international events, participated in this study. Participants 1 and 2 were classified as T54, Participants 3 and 4 as T53, and Participants 5 and 6 as T52. Their 100-m personal best times, body mass, and racing wheelchair mass are summarized in Table 2. Across all participants, the mean ± SD values were 16.34 ± 2.07 s for 100-m personal best time, 59.1 ± 9.7 kg for body mass, and 9.7 ± 1.0 kg for wheelchair mass. Athletes in the T54 class have partial or full trunk function, whereas those in the

Table 1. Overview of representative wheelchair propulsion studies.

Author (Year)	Measurement Target	Measurement Method	Environment	Event Detection	Own Equipment
Ridgway et al. (1988)	Temporal Kinematic	High-speed film	Competition (800-m)	Visual inspection	Yes
Rodgers et al. (1994)	Temporal Physiological	Instrumented wheelchair + 2D + EMG	Laboratory (roller, fatigue test)	Force-based detection	No
Wang et al. (1996)	Temporal	Electronic timing device	Laboratory (roller)	Contact-based detection	Yes
Wong et al. (2007)	Temporal Kinematics	Electro goniometers	Overground (100 m race)	Frequency-based (elbow flexion)	Yes
Poulet et al. (2023)	Temporal Kinematics	IMUs (rear wheels + trunk)	Overground (400 m race)	Visual inspection	Yes
Hikosaka et al. (2024)	Temporal Kinetic	Torque meters + MoCap	Simulator	Torque-based detection	Yes
Ouellet et al. (2025)	Temporal Kinematic	IMU + Lidar	Overground (36m)	Wheelchair translational acceleration	Yes
This study	Kinematic (wheel speed, Glove acceleration vector)	Dual-IMU system	Overground	Glove angular velocity	Yes

Propulsion Condition: Type of environment in which propulsion was measured.
Instrumentation: Devices and systems used to collect biomechanical data.
Event Detection: Method used to identify key push events or push cycle phases.
Own Equipment: Indicates whether athletes used their personal racing wheelchair.

Table 2. Participant characteristics and 100-m performance.

No.	Class	Personal Best (s)	Body Weight (kg)	Wheelchair Weight (kg)
1	T54	13.93	47.5	9.6
2	T54	15.60	59.0	10.5
3	T53	15.42	57.5	8.1
4	T53	15.30	50.5	9.6
5	T52	18.34	73.0	11
6	T52	19.43	67.0	9.4
mean ± SD		16.34 ± 2.07	59.1 ± 9.7	9.7 ± 1.0

T53 and T52 classes present varying degrees of limitations in trunk and upper-limb control [14]. All eligible athletes were contacted in advance via email, provided with written information about the study, and gave electronic informed consent. Participation was confirmed when athletes replied with explicit written consent.

Given the limited number of elite wheelchair sprinters available for field-based research, the sample size reflects the practical constraints of recruiting internationally competitive athletes. Therefore, this study is positioned as a methodological feasibility investigation, rather than a population-level statistical analysis.

2.2. Device

The Sensor-in-Glove System (SIGS) consists of two commercially available 9-axis wireless motion sensors (Logical Product Co., Ltd.). IMU1 (LP‐WSD1215‐0A), a waterproof miniature unit, was embedded inside the rigid glove to measure hand kinematics. IMU2 (LP‐WSV201), a thin-profile sensor, was attached to the inner surface of the racing wheel with its z-axis aligned to the wheel's rotational axis to record wheel rotation. This configuration allowed the two sensors to capture hand and wheel motion within a unified measurement framework, as illustrated in Figure 1A.

IMU1 includes tri-axial accelerometers (± 16 g), gyroscopes (± 1500 dps), and magnetometers, all with 16-bit resolution. The unit weighs approximately 20 g, allowing integration into the glove without affecting push mechanics. IMU2 contains tri-axial accelerometers (± 4/± 8/± 16 g selectable), gyroscopes (± 250…2000 dps), and a tri-axial magnetometer, also with 16-bit resolution. The device weighs 25 g and supports sampling frequencies up to 1000 Hz, providing sufficient temporal resolution for push cycle-wise analysis. IMUs with comparable sampling performance and measurement accuracy have been validated for wheelchair court sports, demonstrating sufficient capability to capture rapid changes in speed and acceleration during propulsion [15]. The detailed specifications of both IMUs are summarised in Figure 1B.

To synchronize the two IMUs, a wireless trigger signal from a pulse generator (LP-WSY12) initiated logging on both sensors simultaneously. Because both units received the same trigger and sampled at 200 Hz, the relative timing offset was structurally constrained to within one sampling interval (5 ms), ensuring reliable alignment of hand and wheel kinematics. This synchronization approach also allowed each IMU to operate independently using its internal logging function, preventing data loss even when wireless communication temporarily weakened during outdoor measurements.

A wheel-based coordinate system (Xw, Yw, Zw) was defined for IMU2, with the Zw-axis aligned to the wheel's rotational axis.

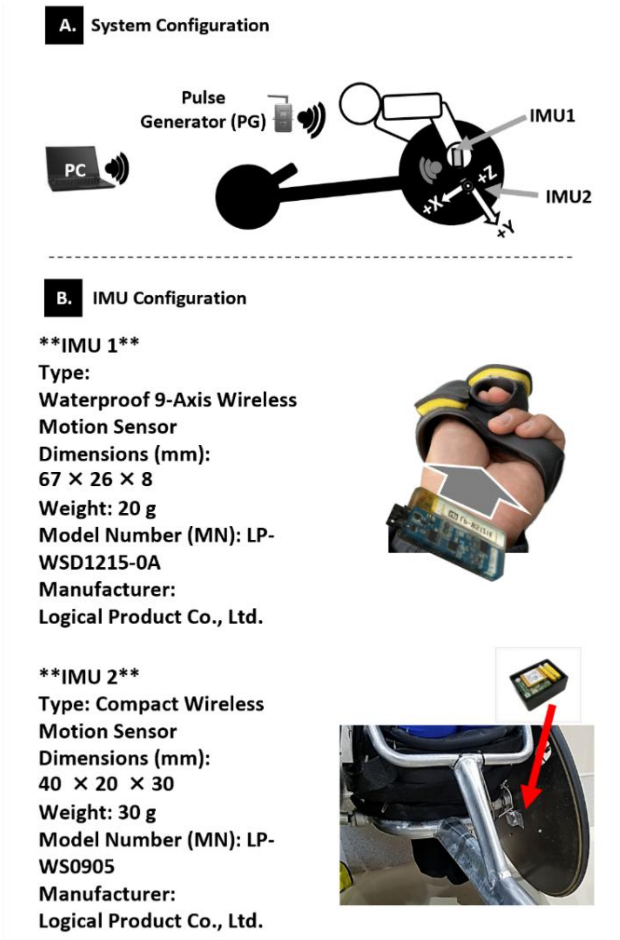

Figure 1. System configuration and IMU specifications. (A) Overview of the Sensor-in-Glove System (SIGS). One IMU (IMU1) is embedded in the glove to record hand motion, while a second IMU (IMU2) is mounted on the wheel to capture wheel rotation. Both IMUs transmit data wirelessly to a PC, and a pulse generator is used for synchronisation. (B) Specifications of the two IMUs used in this study.

A PC equipped with dedicated control software communicated with the pulse generator to initiate measurements and monitor device status. Once triggered, both IMUs recorded data continuously throughout the sprint, enabling full-length acquisition of hand and wheel motion under real-race conditions.

All IMUs were oriented according to a right-handed coordinate system to ensure consistent interpretation of acceleration and angular velocity across sensors.

2.3. Hand-rim contact detection method

In this study, 'push' refers to the hand-rim driving action performed by the athlete, whereas 'propulsion' refers to the forward movement of the wheelchair.

All kinematic data from the glove-mounted IMU (IMU1) were expressed in the glove-based local coordinate system (Figure 2A). Push events were identified by comparing angular-velocity waveforms from IMU1 and IMU2 with synchronised high-speed video. Peaks, zero-crossings, and abrupt waveform changes were matched to corresponding movements, enabling reliable identification of push phases.

Previous studies by Cooper, Higgs, and Morse conceptually divided the push cycle, as detailed in [8], but no objective criteria for phase segmentation had been established. With SIGS, events such as hand contact, propulsion onset, and hand release can be detected directly from waveform features, independent of

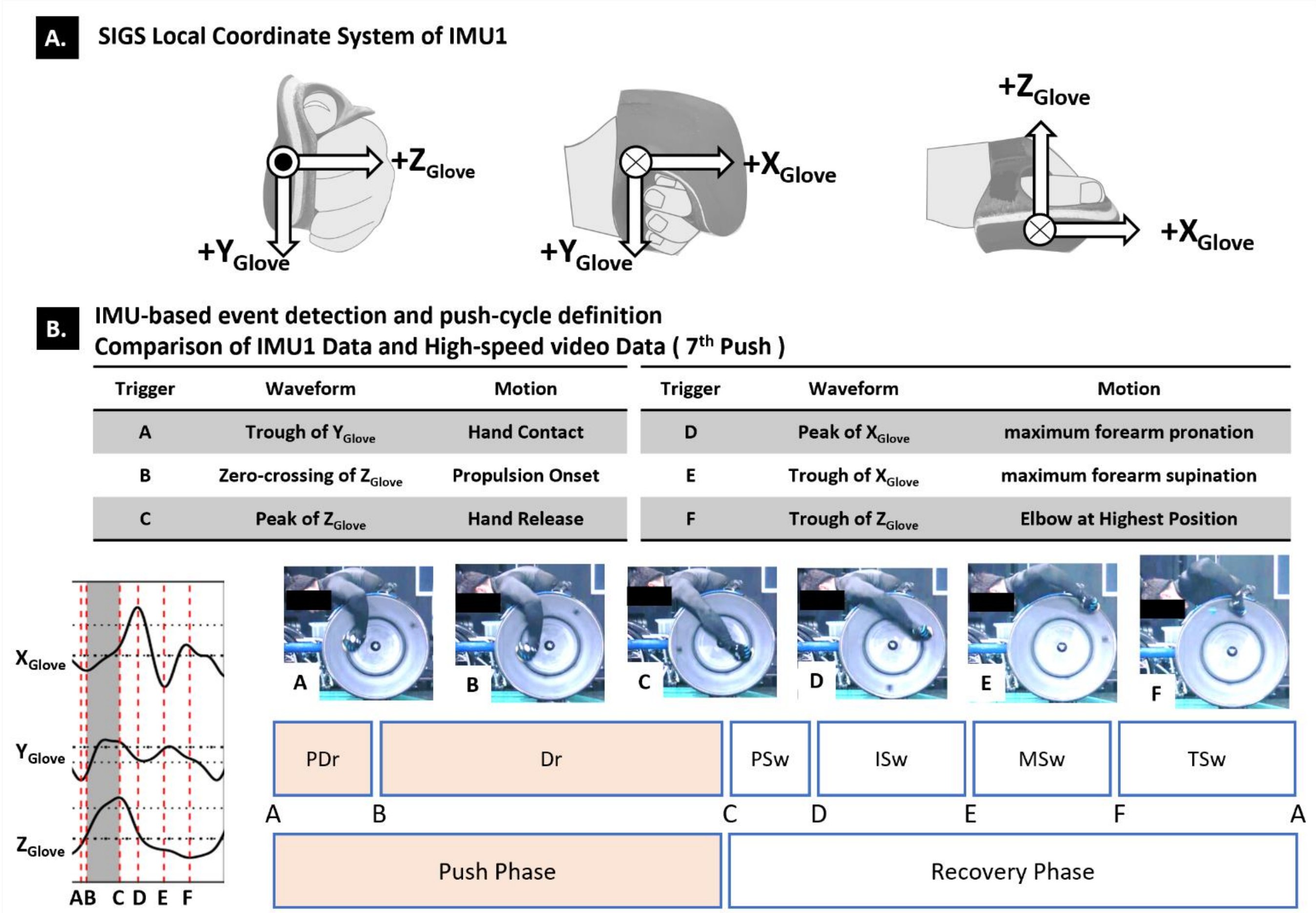

Figure 2. Local coordinate system of IMU1 and correspondence between IMU-derived events and high-speed video. (A) Local coordinate system of the glove-mounted IMU1. (B) Angular-velocity waveforms and synchronized high-speed video frames from the seventh push cycle. Events A–F extracted from IMU signals show consistent correspondence with the video-derived movements (hand contact, propulsion onset, hand release, pronation peak, supination peak, and elbow-highest position). PDr: Pre-Drive, Dr: Drive, PSw: Pre-Swing, ISw: Initial Swing, MSw: Mid Swing, TSw: Terminal Swing.

disability level or measurement environment, enabling objective phase definition for the first time.

Figure 2B presents the angular-velocity waveform from the seventh push cycle, selected because early cycles had small amplitudes and low visibility. Key kinematic events—hand contact, propulsion onset, hand release, pronation, supination, and elbow-highest position—showed consistent alignment between IMU signals and video-derived phases.

Propulsion Onset (PO) was defined as the moment when the hand begins to generate effective forward torque on the handrim. PO was detected using the zero-crossing of the z-axis angular velocity of IMU1:

$$\omega_{\mathrm{z}}^{\mathrm{hand}}(t_{\mathrm{PO}}) = 0\,, \tag{1}$$

$$\frac{d\omega_{\mathrm{z}}^{\mathrm{hand}}}{dt}|t_{\mathrm{PO}} > 0\,, \tag{2}$$

where $\omega_{\mathrm{z}}^{\mathrm{hand}}$ is the angular velocity around the glove-based z-axis.

Hand Release (HR) was defined as the peak of the z-axis angular velocity following PO:

This peak represents the moment when the hand's forward rotational contribution to the wheel is maximal, after which the hand detaches from the rim. This definition was consistent, across participants, and closely matched visually identified release timing. Across all analysed push cycles, each visually identifiable push cycle corresponded to a single PO and HR detected by the IMU-based algorithm, with no missed or spurious events. IMU-based detection showed complete agreement with video annotations (100 %), confirming the procedure's reliability and enabling an objective definition of the wheelchair push cycle.

2.4. Outcome measures

To characterise the biomechanical strategies employed by athletes during the push phase, several kinematic outcome measures were derived from the tri-axial acceleration signals recorded by the glove-mounted IMU (IMU1). Figure 3A illustrates a representative acceleration waveform, and indicates the locations of Propulsion Onset (PO) and Hand Release (HR), which define the interval from which the outcome measures were computed. Figure 3B shows the corresponding moments in the athlete's actual push motion, providing visual confirmation of the kinematic events identified from the IMU signals. All acceleration values were expressed in SI units (m/s²), and all axes were oriented according to the right-handed glove-based coordinate system shown in Figure 3C.

$$t_{\mathrm{HR}} = arg\max_{t>t_{\mathrm{PO}}} \omega_{\mathrm{z}}^{\mathrm{hand}}(t)\,. \tag{3}$$

In this coordinate system, the x- and y-axes represent the tangential plane of the handrim, capturing the primary

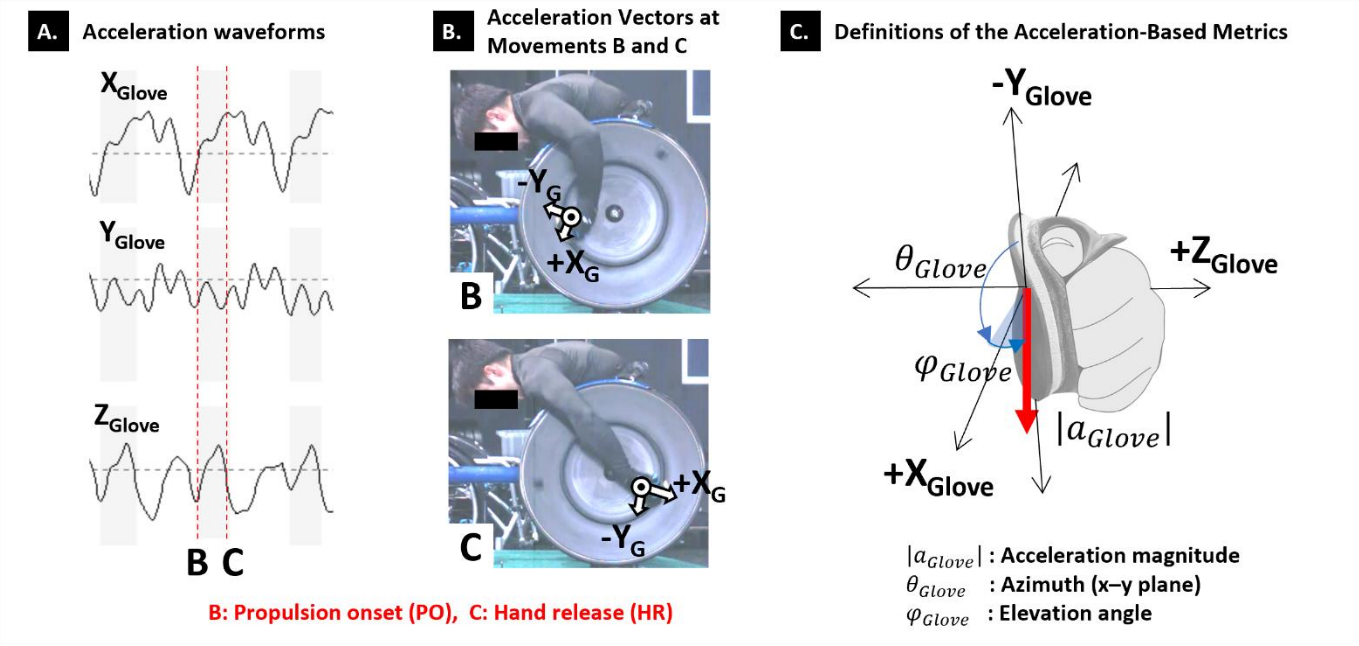

Figure 3. Acceleration waveforms, vector orientation, and definitions of acceleration-based metrics. (A) Acceleration waveforms of IMU1 along the axes during a push cycle. Vertical dashed lines indicate propulsion onset and hand release. (B) Acceleration vectors at propulsion onset and hand release, illustrating the orientation of the axes components relative to upper-limb posture during wheelchair propulsion. (C) Definitions of the acceleration-based metrics used in this study. The acceleration magnitude and its directional components are shown together with the azimuth angle (x–y plane) and elevation angle, which characterise the direction of force application.

circumferential components of hand motion, whereas the z-axis represents the mediolateral direction, corresponding to axial pressure applied toward or away from the wheel. These continuous time-series signals provide a direct description of how acceleration is generated and distributed throughout the push phase.

< Resultant acceleration magnitude >

To evaluate the overall intensity of force application, the magnitude of the resultant acceleration vector $\bar{a}$ was computed using the Euclidean norm.

$$|\vec{a}| = \sqrt{a_{\mathrm{x}}^2 + a_{\mathrm{y}}^2 + a_{\mathrm{z}}^2}\,. \tag{4}$$

This measure reflects the instantaneous three-dimensional intensity of hand motion, and serves as a surrogate for the total mechanical demand during propulsion. Although acceleration is not equivalent to force, it provides a valid proxy for the direction and timing of force application, particularly in field-based measurements, where direct force sensing is not feasible. This approach is consistent with previous IMU-based biomechanical studies.

< Angular orientation of the acceleration vector >

To analyse the directional strategy of force application, two angular indices were computed at the moment of peak resultant acceleration within each push cycle.

< Azimuth angle ($\boldsymbol{\theta}_{\mathbf{Glove}}$) >

The azimuth angle represents the orientation of the acceleration vector within the tangential (x–y) plane:

$$\theta_{\mathrm{Glove}} = \arctan\left(\frac{a_{\mathrm{y}}}{a_{\mathrm{x}}}\right). \tag{5}$$

This angle represents the radial–ulnar direction within the local coordinate system, and indicates the balance between forward and upward/downward components of hand motion.

< Elevation angle ($\boldsymbol{\varphi}_{\mathbf{Glove}}$) >

The elevation angle quantifies the axial contribution relative to the tangential components:

$$\varphi_{\mathrm{Glove}} = \arctan\left(\frac{a_z}{\sqrt{a_x^2 + a_y^2}}\right). \tag{6}$$

This angle represents the dorsiflexion–palmarflexion direction within the local coordinate system. Although it does not directly contribute to forward propulsion, it may reflect individual technique or compensatory movements related to impairment.

Together, the resultant magnitude, and the azimuth and elevation angles provide a comprehensive description of the scale and three-dimensional spatial orientation of the applied acceleration at the peak of each push. These vector-based metrics enable the identification of characteristic push signatures across impairment classes and between individual athletes.

2.5. Experiment protocol

All measurements were conducted on a standard 400-m outdoor track under clear and dry weather conditions. The ambient temperature during data collection ranged from 16.2 °C to 18.1 °C, and the relative humidity varied between 46 % and 58 %. The track surface was a synthetic tartan track. Although wind speed was not instrumentally measured, the conditions were subjectively calm with no noticeable airflow, and thus wind effects on propulsion mechanics were considered negligible.

Each athlete performed a single maximal-effort 100-m sprint using their own racing wheelchair and an experimental glove of the same design as their personal glove, in which IMU1 was embedded (Figure 4). A single-trial protocol was adopted for two reasons. First, maximal sprinting imposes substantial physical demand on wheelchair racing athletes, particularly those in impairment classes T52 and T53, making repeated maximal trials impractical and potentially unsafe. Second, the primary aim of this study was to evaluate the feasibility and validity of the Sensor-in-Glove System (SIGS) during real-race conditions rather than to assess within-subject variability. Therefore, a single representative maximal sprint was sufficient to capture the propulsion characteristics relevant to the study objectives.

The start procedure followed the same protocol used in competition, with the sound emitted by the pulse generator serving as the equivalent of the starting gun. To familiarize themselves with this procedure, the athletes practiced it before the measurement.

After confirming that both IMUs were functioning and synchronised, the wheel-mounted sensor was installed with its z-axis aligned to the wheel's rotational axis. A wireless start signal sent from the PC triggered the pulse generator, which emitted both an auditory and visual cue. To replicate actual 100-m race conditions, athletes were instructed to perform the trial as if competing.

Angular velocity data were recorded at a sampling frequency of 200 Hz [16]. Two experimenters were present during data collection: one operated the PC at the start line, and the other recorded the first 10-m segment with a high-speed camera to validate the IMU-based displacement estimation. The 100-m sprint time was derived from IMU2 by estimating forward displacement from wheel rotational velocity.

During the 100-m trial, the first 10 m were recorded with a high-speed camera synchronized with the IMU data. Synchronization was achieved by positioning the pulse-generator lamp so that its illumination appeared in the video. A calibration was performed for all participants to verify displacement estimation. From the video, the time to reach 10 m was calculated and compared with the IMU-estimated displacement over the same interval.

2.6. Data analysis

The data logged on each IMU were exported to a PC via a wired connection using dedicated software. To reduce high-frequency noise, the signals were processed using a 10-Hz low-pass Butterworth filter. This cutoff frequency has been widely adopted in previous biomechanical studies analyzing wheelchair propulsion and IMU-based acceleration signals [16].

In addition to this methodological consistency, the suitability of the 10-Hz cutoff was verified using frequency-domain analysis of the raw angular velocity data. A fast Fourier transform (FFT) revealed clear spectral peaks at 1–3 Hz corresponding to the push cycle, with the vast majority of signal power concentrated below 5 Hz. In contrast, components above 10 Hz were dominated by vibration- and impact-related noise (Figure 5). Based on these findings, the 10-Hz cutoff was deemed appropriate for preserving biomechanically meaningful signal components while effectively attenuating high-frequency noise.

Smoothing was performed using a third-order polynomial regression. Higher-order models (fourth- and fifth-order) were also tested, but they produced no meaningful changes in the fitted curves, indicating that the third-order model adequately captured the essential structure of the acceleration data. This approach reduced high-frequency noise while preserving local

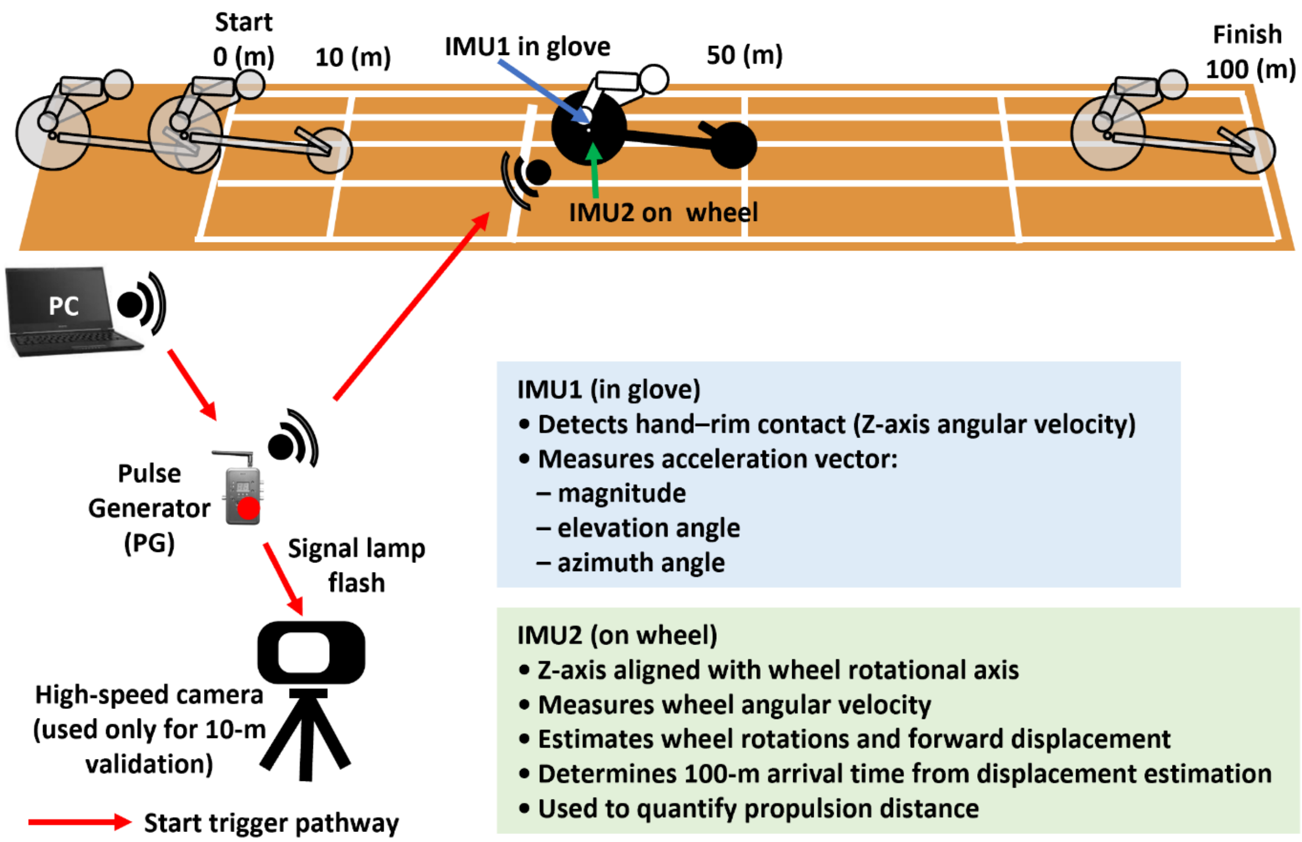

Figure 4. Experimental protocol and measurement system. Athletes performed a maximal-effort 100-m wheelchair sprint, while two IMUs recorded hand and wheel kinematics. IMU1, embedded in the glove, detected hand–rim contact using z-axis angular velocity and measured the three-dimensional acceleration vector. IMU2, mounted on the wheel with its z-axis aligned to the rotational axis, measured wheel angular velocity to estimate wheel rotations, forward displacement, propulsion distance, and the moment the wheelchair reached 100 m. A wireless start signal from the PC activated the pulse generator and synchronised devices. A high-speed camera was used only for validating IMU-based displacement estimation over the initial 10-m segment.

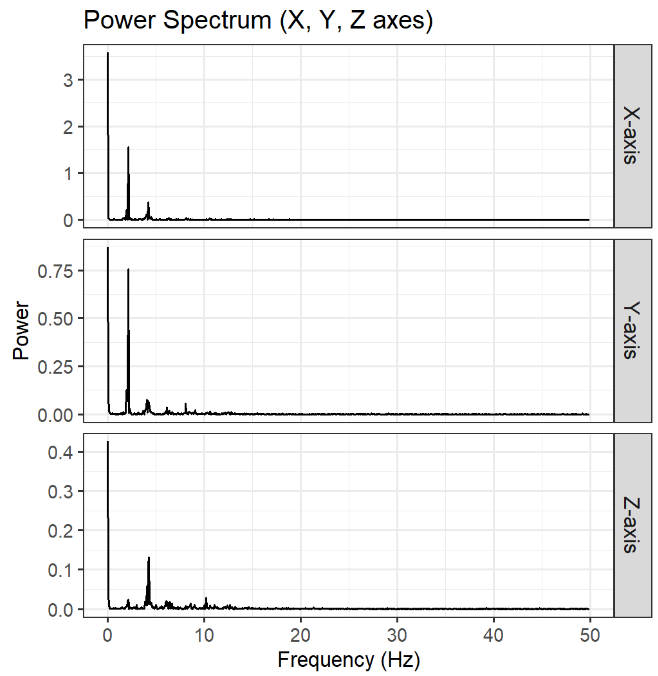

Figure 5. Power spectra of the raw angular velocity signals in the x−, y-, and z-axes. FFT analysis showed that push-related signal power was concentrated below approximately 10 Hz, with higher-frequency components primarily reflecting vibration and noise. Based on these spectra, a 10-Hz low-pass filter was selected for subsequent data processing.

fluctuations, enabling stable estimation of push cycle-wise acceleration patterns.

To enable a detailed analysis of the 100-m sprint, the entire sprint was partitioned into four sections (Figure 6). Wheelchair displacement, velocity, and acceleration were computed from the angular velocity measured by IMU2 mounted on the wheel. Since the characteristics of wheelchair acceleration per push vary between subjects and change depending on the experimental environment—such as indoor ergometer use versus outdoor propulsion—the acceleration profiles were normalized using the maximum acceleration observed during the sprint, and the resulting normalized values are presented as %ACC in Figure 6.

Figure 6 illustrates the 100-m sprint results of a representative subject who performed 31 push cycles. Based on the scatter plot in Figure 6 (middle), the acceleration of the second push cycle was the maximum; therefore, each push cycle was normalized relative to this value and fitted using a logarithmic approximation. The sprint was then segmented into four distinct phases based on the criteria table shown in the figure: the start phase (SP), corresponding to the first two to three push cycles; the initial acceleration phase (IAP), extending to approximately 30 m; the second acceleration phase (SAP), from 30 to 50 m; and the steady-state phase (SSP), beyond 50 m. Based on the criteria shown in Figure 6 (top), the 31 push cycles in this example consisted of 3 push cycles in SP, 12 push cycles in IAP, 5 push cycles in SAP, and 11 push cycles in SSP.

3. RESULTS

The peak resultant acceleration magnitude obtained from IMU1 differed significantly across impairment classes, as confirmed by a one-way ANOVA ($F = 10.52$, $p < 0.001$). Athletes in class T54 exhibited the highest acceleration magnitudes, followed by those in T53 and T52. The class-wise mean $\pm$ SD values were 9.63 $\pm$ 3.77 m/s² for T54, 8.17 $\pm$ 3.27 m/s² for T53, and 7.19 $\pm$ 2.41 m/s² for T52. Post-hoc Tukey tests indicated significant differences between all class pairs (T54 > T53 > T52, all $p < 0.05$), demonstrating that athletes with greater trunk function generated larger peak accelerations during push.

Across all participants, the SIGS-estimated displacement over the 10-m interval was as follows: P1, 9.93 m; P2, 10.16 m; P3, 9.96 m; P4, 10.07 m; P5, 10.06 m; and P6, 9.96 m. These values were obtained by identifying, from synchronised video, the time at which the wheelchair crossed the 10-m mark, and calculating the distance travelled by the wheel during the same period using angular-velocity data from IMU2. The mean absolute error was 7.3 cm (0.73 %), with a maximum positive deviation of 16 cm (1.6 %), indicating that the measurement accuracy was sufficient for subsequent analyses of propulsion and energy characteristics.

Figure 5 to Figure 7 present acceleration waveforms for the X_{Glove}, Y_{Glove}, and Z_{Glove} axes across the four propulsion phases. The horizontal axis represents normalised push time (%) from 0 % to 100 %, and the vertical axis represents acceleration (m/s²) along each respective axis. Each subplot displays smoothed acceleration curves for two participants within the same

Propulsion Phase	Ergometer	Track
Start Phase (SP)	%Acc. >=50	%Acc. >=50
Initial Acceleration Phase (IAP)	%Acc. >=15	%Acc. >= 15
Second Acceleration Phase (SAP)	%Acc. >= 4	%Acc. >= 7
Steady State phase (SSP)	%ACC. < 4	%Acc. < 7

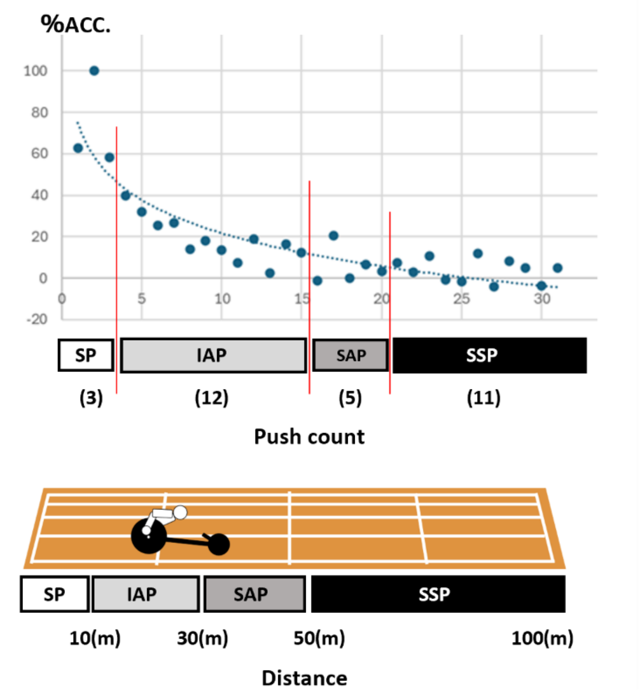

Figure 6. Conceptual illustration of the four segmentation phases. Top: Reference table used to classify the four phases based on normalised acceleration. Mid: Scatter plot showing the relationship between push cycle count (horizontal axis) and normalised acceleration (vertical axis). The example shown represents data from a 100-m sprint completed in 31 push cycles. Wheelchair acceleration was calculated from IMU2 and normalised to the maximum value, which occurred during the second push cycle. Bottom: Approximate distances corresponding to each of the four phases.

impairment class, with shaded regions indicating 95 % confidence intervals. These figures provide an overview of axis-specific acceleration behaviour prior to the detailed class-wise comparisons described below.

Acceleration characteristics for each impairment class were then examined across the propulsion phases (Figure 5 to Figure 7). In each class, the participant with the higher velocity is shown in blue, and the slower participant in red. Solid lines represent smoothed acceleration curves, and shaded regions denote 95 % confidence intervals.

As wheelchair velocity increased, acceleration values rose across all axes. The T54 and T53 classes exhibited broadly similar waveform characteristics, whereas the T52 class showed distinctly different patterns, reflecting greater functional limitations. The X_{Glove} and Y_{Glove} axes, which correspond to the tangential components directly contributing to wheel rotation, demonstrated increasing peak accelerations as the propulsion phases progressed.

For the X_{Glove} axis (Figure 7), the overall waveform shapes were similar across classes, yet peak magnitudes and timings varied between participants, reflecting individual push strategies. In the T54 class, Participant 1, who achieved the highest velocities across all phases, displayed a predominantly linear increase in acceleration. In contrast, Participant 2, whose velocity did not rise sufficiently during SP and IAP, exhibited a more curved pattern. This suggests that a more linear increase in X_{Glove} axis acceleration may contribute to superior propulsion performance. A similar tendency was observed in the T53 class: Participant 3 showed a curved pattern during SP, corresponding to lower velocity, but demonstrated a more linear pattern in later phases, which coincided with improved speed. Participant 4 showed curved patterns throughout, consistent with lower velocity, similar to Participant 2. Although Participant 3 exhibited some linearity, the waveform contained greater curvature than that of Participant 1, which may explain the performance difference. In the T52 class, functional limitations resulted in waveform patterns that differed markedly from those of T54 and T53, with curved profiles dominating across all phases. Participant 5 produced larger acceleration values and achieved higher velocities than Participant 6, suggesting that differences emerging particularly in the SAP and SSP phases contributed substantially to performance disparities.

The Y_{Glove} axis (Figure 8) also showed broadly similar patterns across participants, although all waveforms were curved, unlike those of the X_{Glove} axis. Larger amplitude variation within the waveform appeared to be associated with better performance, with Participant 1—who exhibited the greatest amplitude range—achieving the highest velocity overall. Both the X_{Glove} and Y_{Glove} axes showed increasing acceleration from 0 % to 100 % Push Time, indicating that coordinated increases in both axes contribute to higher propulsion performance. A smooth increase in X_{Glove} acceleration in the positive direction and Y_{Glove} acceleration in the negative direction appeared particularly desirable, and this coordinated pattern was most clearly demonstrated by Participant 1, whose maximum acceleration occurred just before hand release (HR), likely contributing to efficient propulsion. Notably, the waveforms of T54 and T53 participants with similar performance levels were highly alike, and in both classes, larger negative Y_{Glove} values at HR were associated with higher wheelchair velocity. This suggests that, as with the X_{Glove} axis, having the peak acceleration occur later in the Push Time (%) may be advantageous for achieving higher speeds.

The Z_{Glove} axis (Figure 9) exhibited the greatest variability among participants, reflecting individual push characteristics more strongly than the other axes. While SAP and SSP showed broadly similar patterns across participants, the IAP phase displayed distinctive waveform features for each athlete. During SP and IAP, wheelchair velocity is relatively low, reducing the need to minimise deceleration caused by glove–rim contact. Consequently, athletes tended to maintain longer and stronger contact with the handrim, which may explain why individual push strategies were more clearly reflected in the Z_{Glove} axis during IAP. Because the Z_{Glove} axis represents the mediolateral component, which does not contribute directly to wheel rotation, smaller values are generally desirable. However, Participant 4 displayed a unique pattern, with a peak around 25 % Push Time followed by a gradual decrease, clearly differing from the other athletes. The divergence of waveform direction around 25 % and 50 % Push Time further suggests that the Z_{Glove} axis captures individual push characteristics more distinctly than the X_{Glove} or Y_{Glove} axes.

4. DISCUSSION

In the Results section, each acceleration axis was examined independently.

However, because push performance is inherently determined by the integrated three-dimensional behavior of the hand, the Discussion focuses on vector-based descriptors of the 3-axis acceleration signal in the glove-embedded coordinate system.

In this study, the timing at which the resultant acceleration reached its maximum within each push cycle was defined as $Peak_{\mathbf{Glove}}$ (%). At this Peak moment, we computed the magnitude $|a_{\mathbf{Glove}}|$, azimuth $\theta_{\mathbf{Glove}}$, and elevation $\varphi_{\mathbf{Glove}}$ of the acceleration vector to characterize the three-dimensional structure of the hand's force-production strategy.

4.1. $Peak_{\mathbf{Glove}}$(%) and velocity

The $Peak_{\mathbf{Glove}}$ (%) calculated in this study represents the timing within a push cycle at which the resultant acceleration reaches its maximum. A value of 0 % corresponds to propulsion onset (PO), when the glove first begins to act on the handrim, and 100 % corresponds to hand release (HR). Figure 10 illustrates the relationship between $Peak_{\mathbf{Glove}}$ (%) and wheelchair velocity. The figure presents a scatter plot with wheelchair velocity on the horizontal axis and $Peak_{\mathbf{Glove}}$ (%) on the vertical axis, and includes the slope of the regression line and the corresponding correlation coefficient.

Across all propulsion phases, no clear correlation was observed between $Peak_{\mathbf{Glove}}$ (%) and velocity. Even at similar velocities, $Peak_{\mathbf{Glove}}$ (%) varied between athletes. Moreover, as the propulsion phases progressed, each participant's $Peak_{\mathbf{Glove}}$ (%) tended to converge towards a stable value. These findings suggest that $Peak_{\mathbf{Glove}}$ (%) reflects individual push style rather than changes in velocity. A comparison of four representative athletes further supports this interpretation. Participants P1 and P3 showed values clustered near 100 % during the SAP and SSP phases, indicating a terminal-type push cycle, in which peak acceleration occurs immediately before HR. In contrast, P2 and P4 exhibited values converging around 50–60 % during SAP and SSP, corresponding to a middle-type push cycle, where peak acceleration occurs in the mid-portion of the contact phase. These results clearly demonstrate the presence of distinct push styles.

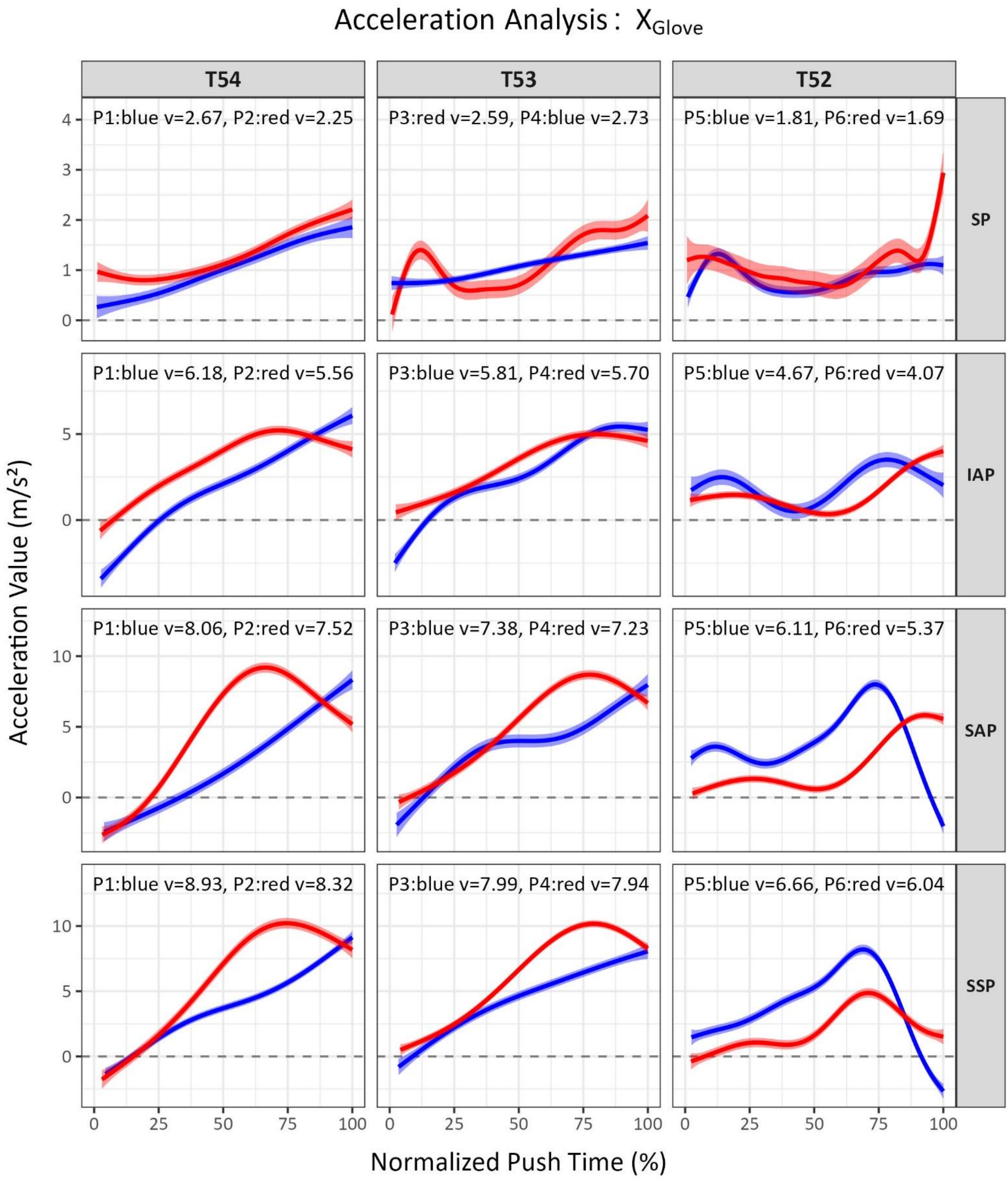

Figure 7. Changes in X_{Glove} -axis acceleration across propulsion phases. This figure shows the variation in x-axis acceleration across the four propulsion phases (SP, IAP, SAP, SSP), categorised by impairment class (T54: P1 and P2; T53: P3 and P4; T52: P5 and P6). The value "v" within each panel represents the mean velocity (m/s) for the corresponding phases.

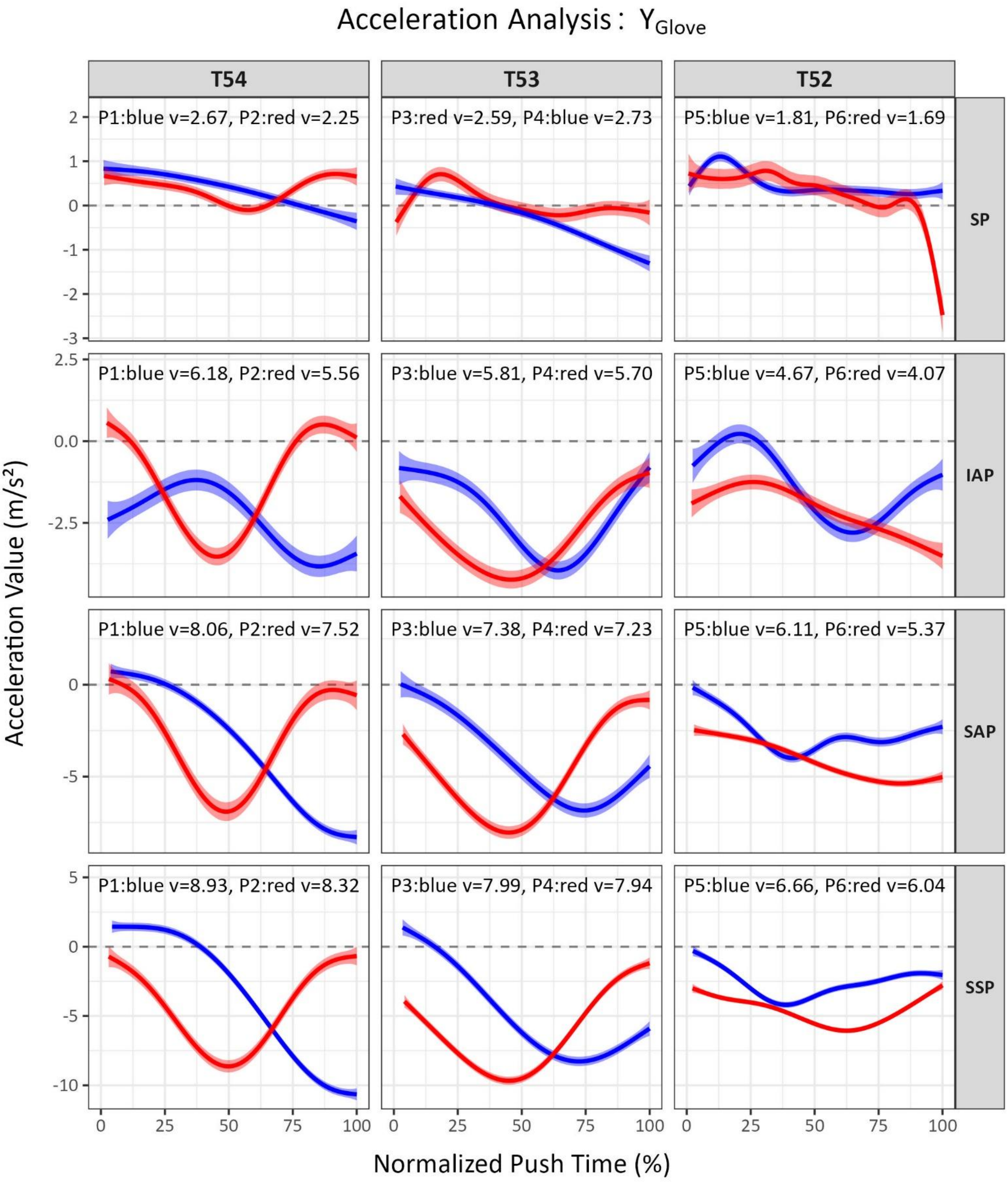

Figure 8. Changes in Y_{Glove} - axis acceleration across propulsion phases. This figure shows the variation in x - axis acceleration across the four propulsion phases (SP, IAP, SAP, SSP), categorised by impairment class (T54: P1 and P2; T53: P3 and P4; T52: P5 and P6). The value "v" within each panel represents the mean velocity (m/s) for the corresponding phases.

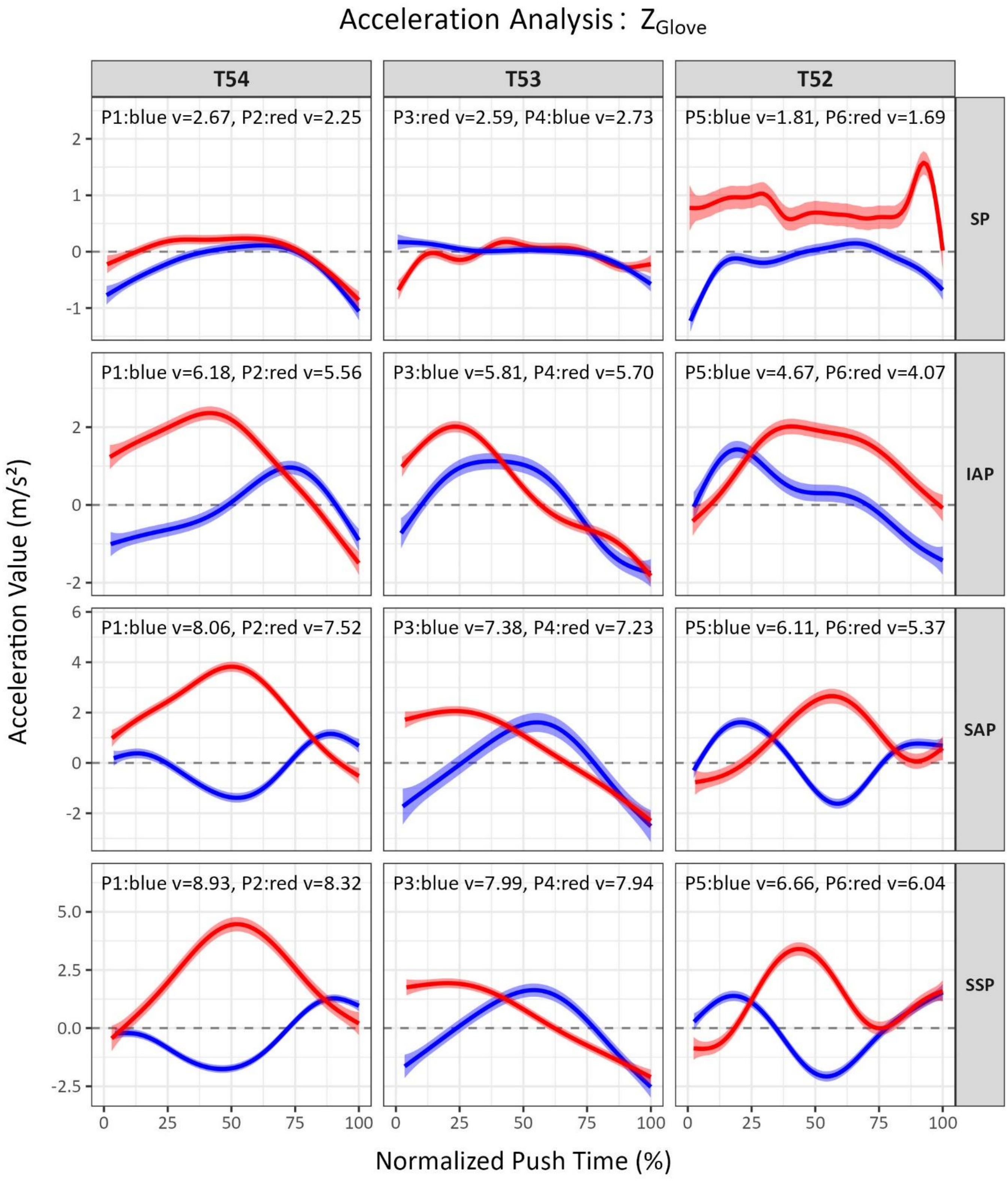

Figure 9. Changes in Z_{Glove} - axis acceleration across propulsion phases. This figure shows the variation in x - axis acceleration across the four propulsion phases (SP, IAP, SAP, SSP), categorised by impairment class (T54: P1 and P2; T53: P3 and P4; T52: P5 and P6). The value “v” within each panel represents the mean velocity (m/s) for the corresponding phases.

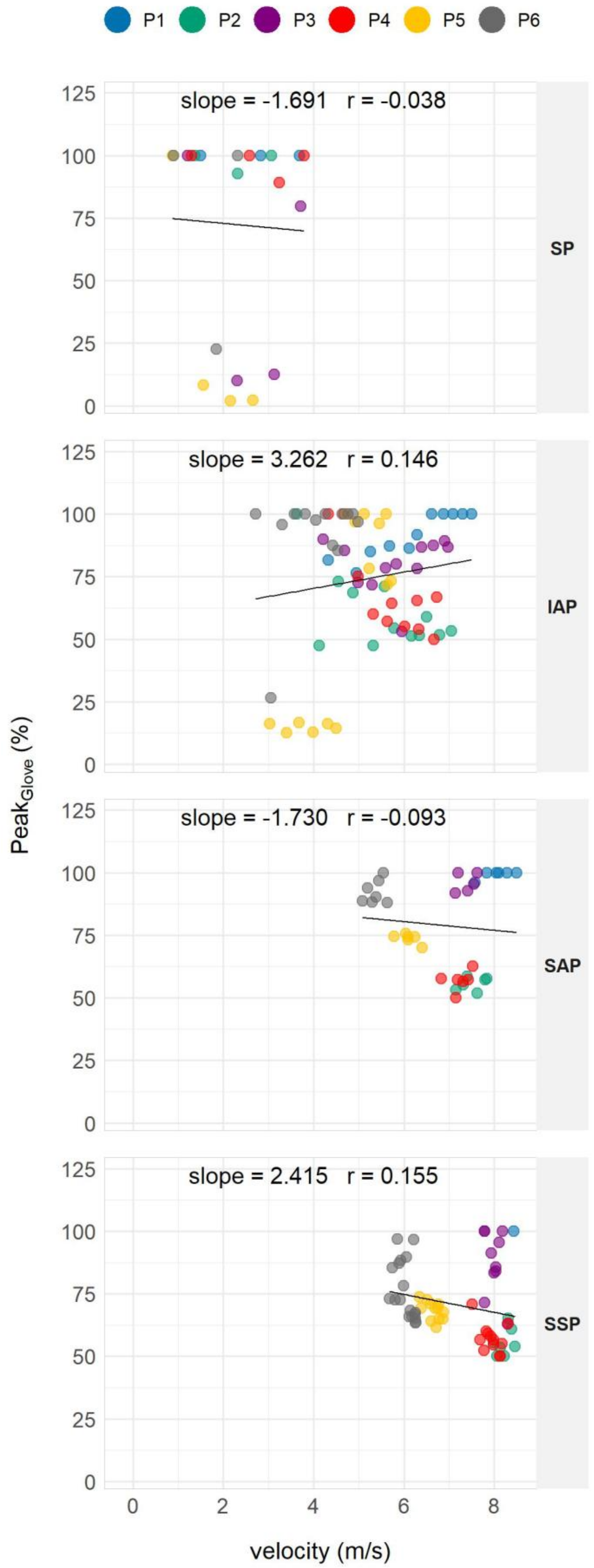

Figure 10. $Peak_{Glove}$ (%) and velocity. Relationship between wheelchair velocity and the timing of peak resultant acceleration, defined as $Peak_{Glove}$ (%) with 0 % at propulsion onset (PO) and 100 % at hand release (HR). Each point represents the timing of peak acceleration across four propulsion phases (SP, IAP, SAP, SSP), with regression lines indicating phase-specific trends.

Participants P1 and P3, who employed terminal-type push cycles with peaks occurring just before HR, achieved faster times than P2 and P4 within the same impairment class. This aligns with previous findings suggesting that producing peak torque at a more posterior position contributes to increased wheel speed [16]. In other words, adopting a terminal-type push cycle—through technique or seat positioning—may enhance wheelchair velocity. However, terminal-type push cycles require advanced skill, as full elbow extension increases the risk of the glove catching on the handrim. Conversely, although P2 (middle-type) reached 8.32 m/s in the SSP, which was lower than P1's 8.93 m/s, P4 achieved 7.94 m/s, only slightly below P3's 7.99 m/s. These observations suggest that each athlete optimises seat position and technique according to their physical characteristics, and that selecting a push type suited to the individual may contribute to improved performance.

Therefore, although $Peak_{\mathrm{Glove}}$ (%) does not directly determine velocity, it serves as a useful biomechanical indicator that characterises an athlete's individual push type.

4.2. Maximum acceleration and velocity

The relationship between wheelchair velocity and the magnitude of the resultant acceleration $|a_{\mathrm{Glove}}|$ at the moment of peak acceleration was examined for each propulsion phase (Figure 11). The results demonstrated that, as the propulsion phases progressed, the correlation between velocity and $|a_{\mathrm{Glove}}|$ strengthened, revealing clearer distinctions in force-production characteristics across impairment classes.

In the start phase (SP), almost no correlation was observed between wheelchair velocity and $|a_{\mathrm{Glove}}|$ (r = 0.113). This may partly be due to the limited number of push cycles available for analysis, as SP typically comprises only the first three to four push cycles from a stationary position. SP represents the initial acceleration phase, during which wheelchair acceleration is greatest, and therefore crucial in short-distance racing. The horizontal dispersion of data points indicates that substantial differences in wheelchair velocity emerge within only a few push cycles. Additionally, SP is strongly influenced by starting technique, trunk stability, and the ability to overcome static inertia, which may obscure the relationship between instantaneous acceleration and velocity.

In the initial acceleration phase (IAP), a strong positive correlation was observed between velocity and $|a_{\mathrm{Glove}}|$ (r = 0.707, $slope$ = 1.383). IAP is the phase in which acceleration becomes fully established, and athletes increase velocity by generating greater propulsive force. In the scatter plot, participants with lower impairment levels (P1 and P2) maintained high acceleration magnitudes at higher velocity ranges, whereas participants with greater impairment (P5 and P6) remained in lower velocity ranges with correspondingly lower peak accelerations. The wide horizontal dispersion—the largest among all phases—indicates that IAP is the phase in which the greatest differences in wheelchair velocity emerge. This phase appears to be particularly sensitive to functional limitations, such as trunk control, shoulder stability, and the ability to maintain consistent handrim contact.

In the second acceleration phase (SAP) and steady-state phase (SSP), the correlation became even stronger (SAP: r = 0.864; SSP: r = 0.913). Notably, the slope was greatest in SSP ($slope$ = 1.714), indicating that $|a_{\mathrm{Glove}}|$ becomes a decisive factor for maintaining or increasing velocity during high-speed propulsion. Participants P1 and P2, who sustained high velocities,

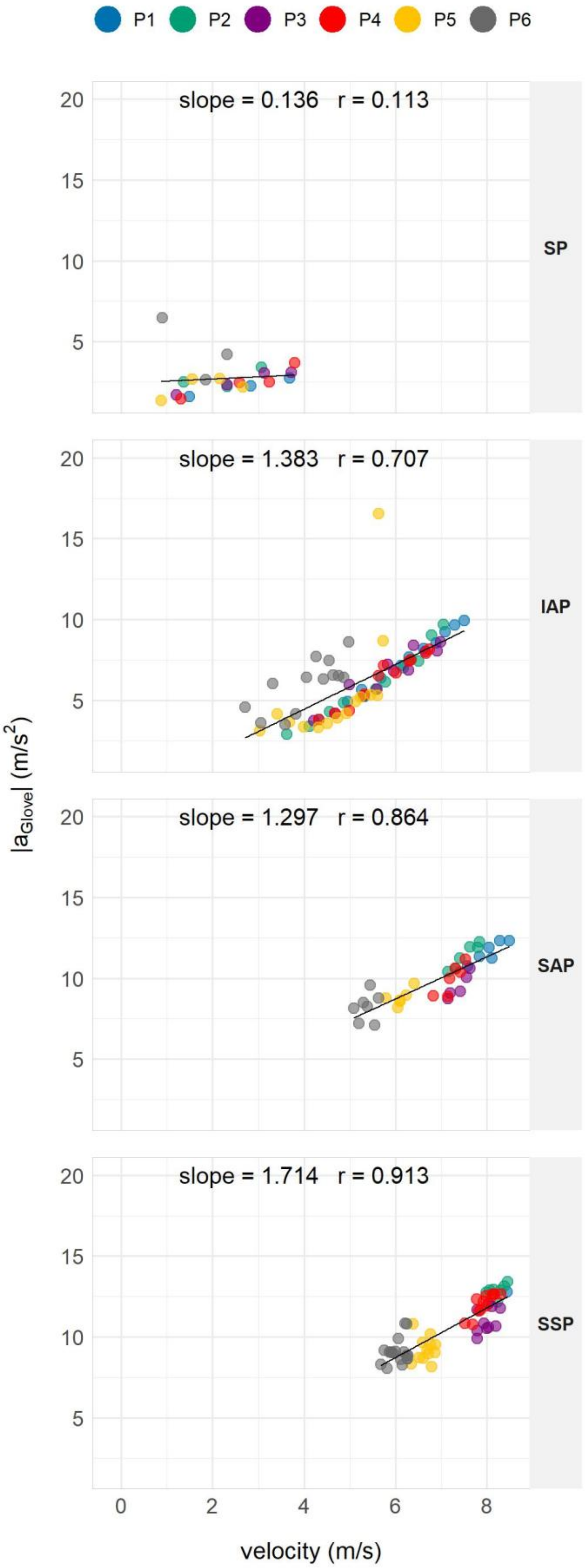

Figure 11. Maximum resultant acceleration and velocity. Relationship between velocity and the magnitude of the resultant acceleration at the moment of peak acceleration across four propulsion phases (SP, IAP, SAP, SSP). Each point represents the maximum acceleration within a push cycle, with regression lines indicating phase-specific trends.

were able to consistently transmit large accelerations to the handrim even at high speeds. In contrast, P5 and P6 showed smaller increases in acceleration with increasing velocity and tended to plateau at approximately 6–7 m/s. Furthermore, the widening velocity gap between the T52 athletes (P5 and P6) and the other participants from SAP to SSP suggests that performance differences attributable to impairment class become more pronounced beyond 50 m. This widening gap likely reflects the cumulative effect of reduced trunk stability and limited upper-limb control, which restrict the ability to generate high-magnitude, directionally efficient acceleration at elevated speeds.

Overall, these findings show that $|a_{\mathbf{Glove}}|$ becomes increasingly informative of physical function and push technique as the phases progress. During high-velocity propulsion, stable force production supported by trunk control appears crucial for sustaining the velocity–acceleration relationship. Thus, acceleration-based metrics offer practical insight into impairment-specific performance, and can guide technique optimisation in wheelchair racing.

4.3. Azimuth and velocity

The relationship between wheelchair velocity and the azimuth angle $\theta_{\mathbf{Glove}}$, derived from the tangential acceleration components (X_{Glove} and Y_{Glove} axes), was examined for each propulsion phase.

In the start phase (SP), $\theta_{\mathbf{Glove}}$ changed markedly as wheelchair velocity increased, shifting from approximately +90° towards –90° (slope = –12.377), (Figure 12). In the initial acceleration phase (IAP), $\theta_{\mathbf{Glove}}$ decreased from around 0° towards –90°, with most values falling within the negative range. This indicates a transition in the direction of force application from the + X_{Glove} axis towards the – Y_{Glove} axis as propulsion progressed from SP to IAP. The wide range of velocities observed during IAP suggests that performance differences among athletes emerge most prominently in this phase. This transition also reflects the shift from trunk-driven downward motion to a more coordinated upper-limb-driven push as athletes adapt to increasing wheel speed.

During low-velocity propulsion in SP, athletes tend to generate maximum acceleration by swinging the glove downward using trunk motion, resulting in force directed primarily along the + X_{Glove} axis. However, as wheelchair velocity increases during IAP, applying force in the same manner would cause substantial resistance when the glove contacts the handrim. Therefore, athletes must time handrim contact such that the downward glove velocity closely matches the rotational velocity of the wheel. This timing coincides with the moment when elbow extension is most effective, causing the direction of force to shift towards the – Y_{Glove} axis.

In the second acceleration phase (SAP) and steady-state phase (SSP), $\theta_{\mathbf{Glove}}$ converged towards values between 0° and the negative range for all participants, and both the correlation and slope became more moderate (SAP: r = -0.244; SSP: r = -0.344). This indicates that at higher velocities, $\theta_{\mathbf{Glove}}$ stabilises, reflecting a consistent direction of force application.

From SAP onwards, athletes in the T52 class (P5 and P6) showed limited increases in velocity, widening the performance gap relative to the other participants. Between the two T52 athletes, P5 demonstrated better performance and exhibited values closer to 0° , indicating force directed more towards the + X_{Glove} axis. This suggests that P5 employed a push cycle

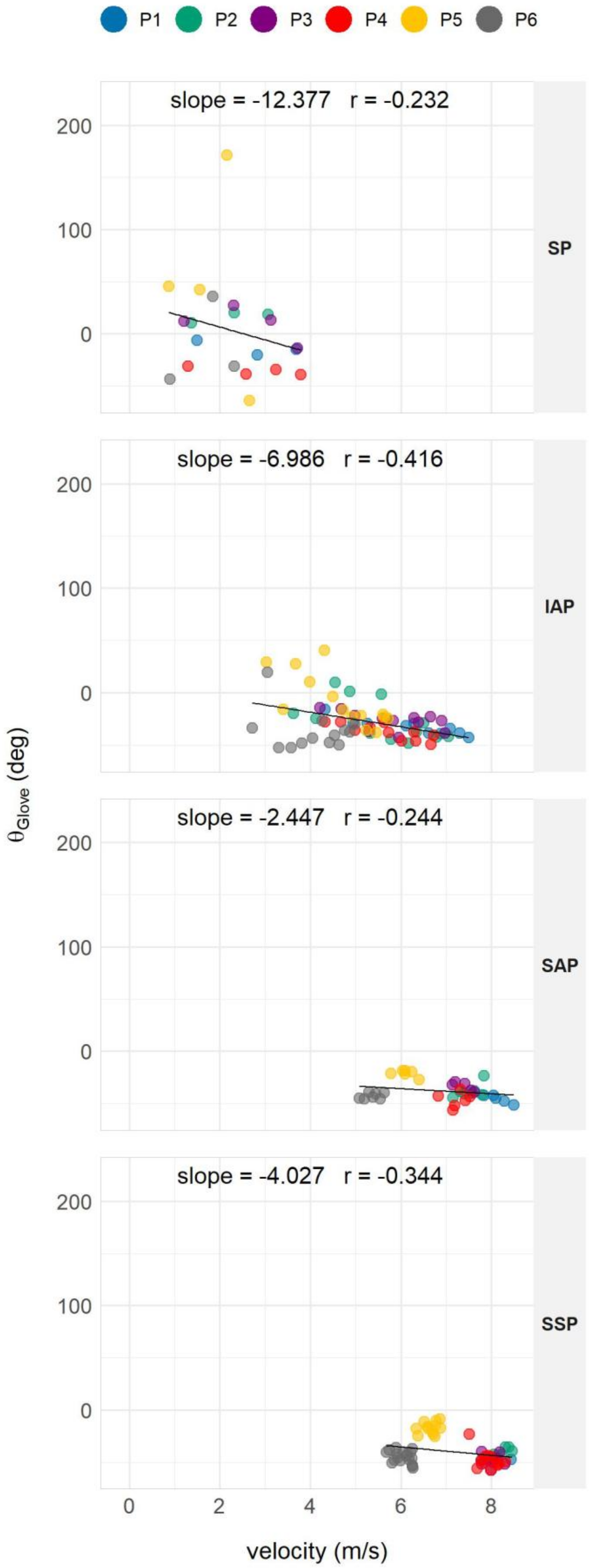

Figure 12. Azimuth angle at maximum acceleration. Azimuth angle at the moment of maximum resultant acceleration plotted against velocity for four propulsion phases. Positive values indicate directions closer to the tangential axis, whereas negative values reflect mid-push positions. Regression lines illustrate phase-dependent directional tendencies.

pattern that effectively utilised elbow extension—a rational strategy given the limited trunk function characteristic of the T52 class. In contrast, P6 appeared to adopt a push cycle pattern similar to those of T54 and T53 athletes, initiating push at a point where elbow extension reduces contact resistance with the handrim. Adjusting the push cycle pattern to better match the functional characteristics of the T52 class may therefore improve performance.

A notable finding is that athletes in the T54 and T53 classes exhibited highly similar θ_{Glove} values during high-velocity propulsion, suggesting that adopting a comparable push cycle pattern contributes to performance in these classes.

Overall, the azimuth angle θ_{Glove} flects qualitative aspects of propulsion—specifically, the direction in which force is applied—that cannot be captured by acceleration magnitude alone. It serves as a valuable indicator of how athletes adjust their push cycle mechanics across propulsion phases and impairment levels, and highlights the importance of matching push strategy to functional capacity.

4.4. Elevation angle and velocity

The elevation angle φ_{Glove}, calculated from the acceleration component along the ZGlove axis, which is perpendicular to the handrim, was examined to clarify how athletes regulate the direction of glove–handrim contact as wheelchair velocity increases (Figure 13). This parameter represents the angle directed from the palmar side towards the dorsal side of the hand at the moment force is applied, with positive values indicating this orientation. It therefore provides important information for evaluating the stability and efficiency of handrim contact.

When φ_{Glove} is close to 0°, it indicates that the glove shape allows force to be transmitted accurately in the tangential direction of the handrim. In contrast, large positive or negative values suggest that part of the applied force is diverted mediolaterally, potentially dissipating energy that does not contribute to wheel rotation.

In the start phase (SP) and initial acceleration phase (IAP), φ_{Glove} was widely dispersed within the negative range (approximately –25° to –75°), and correlations with velocity were extremely low (SP: r = 0.043; IAP: r = –0.099). This suggests that, during the early low-velocity phases, athletes prioritise generating impulse by pressing the glove firmly against the handrim, rather than applying force purely in the tangential direction. Among athletes with greater impairment (P5 and P6), the pronounced negative deviation of φ_{Glove} likely reflects limited trunk stability, causing increased mediolateral force as the glove is pressed against the handrim. This pattern also indicates that early-phase propulsion is strongly influenced by the need to stabilise the upper body and establish a secure glove–rim interface before effective tangential force can be produced.

As propulsion progressed into the second acceleration phase (SAP) and steady-state phase (SSP), a positive correlation emerged between velocity and φ_{Glove} (SAP: r = 0.210; SSP: r = 0.447). The slope was greatest in SSP ($slope$ = 4.448), indicating that athletes who reached higher velocities (8–9 m/s; P1 and P2) tended to converge towards values near or slightly above 0° (0° to +25°). This suggests that maintaining high velocity requires not only accurate tangential force transmission but also the ability to sustain an appropriate glove–handrim contact angle aligned with the wheel's camber until hand release (HR). The narrowing distribution of φ_{Glove} at high speeds further implies that efficient propulsion constrains the range of

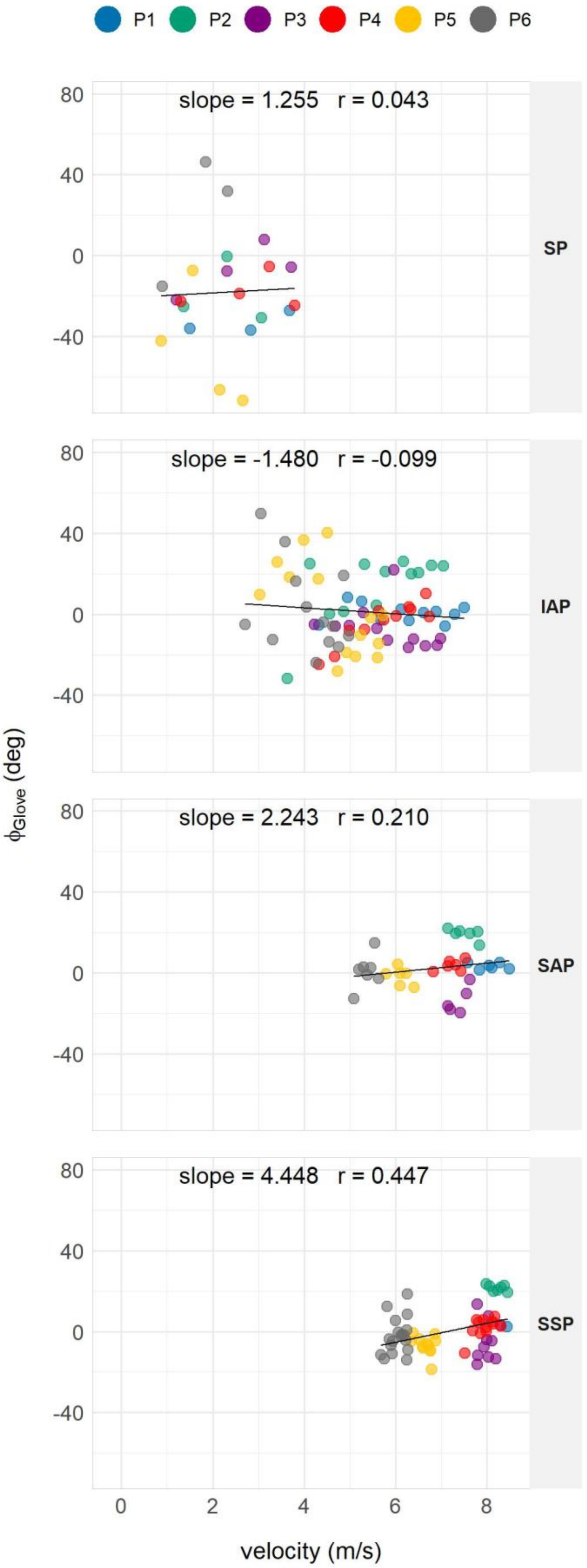

Figure 13. Elevation angle at maximum acceleration. Elevation angle relative to velocity at the moment of maximum resultant acceleration across four propulsion phases. Higher elevation angles indicate greater outward (lateral) acceleration components. Regression lines show how lateral force components vary with speed in each phase.

viable contact angles. Although each participant exhibited convergence toward a specific angle, the converged angle differed among individuals, likely reflecting differences in glove geometry. Participants whose converged φ_{Glove} more closely resembled that of P1—the highest-performing athlete—may therefore benefit from glove shapes that more effectively support efficient propulsion.

The narrowing distribution of φ_{Glove} at high speeds indicates that efficient propulsion is characterised not by a specific angle itself, but by the degree to which the angle remains concentrated around a single, stable value. Such convergence reflects wrist stability, and suggests a push pattern with minimal mechanical loss. In contrast, P6 exhibited the largest dispersion in φ_{Glove}, indicating unstable contact angles and likely greater propulsion loss. The remaining participants showed convergence toward a single angle, implying that their current technique and glove geometry provide a relatively stable interaction with the handrim.

However, even when φ_{Glove} converges to a single value, this does not necessarily mean that the converged angle is optimal for propulsion. Determining whether the angle is truly optimal for generating forward motion requires further consideration of each athlete's physical characteristics, as well as the influence of glove geometry. When analysed alongside $|a_{\text{Glove}}|$ and φ_{Glove} at $Peak_{\text{Glove}}(\%)$, the elevation angle provides a multidimensional understanding of an athlete's push technique and technical proficiency.

4.5. Limitations

This study has several limitations that should be considered when interpreting the findings. First, the sample size was limited to six athletes, with two athletes representing each impairment class (T52, T53, and T54). Although this distribution allowed for preliminary comparison across classes, the small number of participants restricts the generalisability of the observed push characteristics. Given this limited sample size, the present work should be interpreted as a proof-of-concept field validation of the Sensor-in-Glove System. Future studies should include larger cohorts within each class to examine class-specific propulsion strategies with greater statistical power.

Second, only a single maximal-effort 100-m sprint was analysed for each athlete. This protocol was chosen to ensure safety and feasibility, particularly for athletes in classes T52 and T53, for whom repeated maximal trials would impose excessive physical burden. However, this design does not allow assessment of within-athlete variability. Future work should incorporate submaximal or shorter repeated trials to evaluate the consistency of individual push patterns.

Third, although the Sensor-in-Glove System (SIGS) enables field-based measurement under real-race conditions, the system does not directly measure propulsion force. In this study, three-dimensional acceleration was used as a proxy for the direction and timing of force application. While this approach is appropriate for characterising push strategies, integrating SIGS with instrumented wheels or force-sensing gloves would allow direct quantification of mechanical output and improve the interpretation of propulsion efficiency.

Fourth, the present analysis focused on the moment of peak resultant acceleration within each push. Although this metric provides a clear and consistent reference point, push is a continuous process, and additional temporal features—such as the evolution of acceleration direction throughout the push phase—may offer further insight into technique differences among athletes. Future studies should explore time-series modelling approaches to capture the full dynamics of force-orientation strategies.

Finally, the 100-m sprint time was derived from IMU2 by estimating forward displacement from wheel rotational velocity, because no observer was positioned at the finish line. Although this configuration allowed the experiment to be conducted with only two operators and without personnel at the finish line, the accuracy of the 100-m time depends on the displacement estimation accuracy of IMU2. The IMU demonstrated a displacement error of 0.73 % over 10 m, corresponding to approximately 0.73 m over 100 m. Given that wheelchair racing speeds at the finish typically range from 7 to 9 m/s, this displacement error may introduce a timing uncertainty of roughly 0.08–0.10 s. While this limitation affects the absolute 100-m time, it does not substantially influence the primary outcome measures related to propulsion mechanics.

Despite these limitations, the findings demonstrate that SIGS provides a practical and scalable method for capturing three-dimensional hand acceleration during outdoor wheelchair sprinting. The system enables push-wise analysis of propulsion directionality under real-race conditions, offering new opportunities for performance assessment and technique optimisation in wheelchair racing.

5. CONCLUSIONS

This study demonstrated that the Sensor-in-Glove System (SIGS) provides a practical and reliable method for capturing three-dimensional hand acceleration during outdoor wheelchair sprinting. By combining glove-mounted and wheel-mounted IMUs, the system enabled push-wise identification of propulsion onset and release under real-race conditions with high temporal precision. The system achieved a displacement-estimation error of 0.73 % over a 10-m interval, and the vector-based acceleration metrics showed strong correlations with wheelchair velocity (r = 0.82–0.95), indicating that the measured kinematics closely reflect propulsion performance.

The findings revealed class-specific differences in peak resultant acceleration ($F = 10.52$, $p < 0.001$) and demonstrated that athletes exhibit distinct azimuth and elevation angle patterns at the moment of peak acceleration, suggesting individualised force-orientation strategies even within the same impairment class. Although SIGS does not directly measure force, the acceleration-based indices provided a meaningful proxy for the magnitude and direction of applied mechanical demand, offering quantitative insight into propulsion technique that is not accessible through conventional field-based methods.

Overall, SIGS offers a lightweight, portable, and scalable approach for biomechanical assessment in wheelchair racing. Its ability to quantify push-cycle-wise acceleration magnitude and orientation under outdoor sprinting conditions provides new opportunities for evidence-based coaching, technique optimisation, and classification research, supporting future work aimed at athlete-specific performance enhancement.

ACKNOWLEDGEMENT

We thank Dr. Kyungsu Jung and staff at the Wakayama Medical University Center for Future Medical Promotion.

REFERENCES

[1] W. Guo, Q. Liu, P. Huang, D. Wang, L. Shi, D. Han, The effects of trunk kinematics and EMG activity of wheelchair racing T54 athletes on wheelchair propulsion speeds, PeerJ 11 (2023), pp. e15792.
DOI: 10.7717/PEERJ.15792

[2] K. Kawabata, T. Ibusuki, T. Mitsui, Y.-I. Kamijo, F. Tajima, Kinematic analysis of the head and trunk movements of quadriplegic wheelchair athletes in the initial acceleration phase of the 100-m sprint: a case study, Int. Journal of Sport and Health Science 22 (2024), pp. 34–41.
DOI: 10.5432/ijshs.202325

[3] R. A. Cooper, SMARTWheel, Prosthetics & Orthotics International 33 (2009), pp.198–209.
DOI: 10.1080/03093640903082126

[4] M. Hikosaka, T. Kodachi, H. Yamato, N. Kawashima, Novel evaluation tool for wheelchair racing performance: precise adjustment of the wheel axle and torque measurement during wheelchair propulsion, Int. Journal of Sport and Health Science 22 (2024), pp. 123–129.
DOI: 10.5432/ijshs.202407

[5] Y. Poulet, F. Brassart, E. Simonetti, H. Pillet, A. Faupin, C. Sauret, Analyzing intra-cycle velocity profile and trunk inclination during wheelchair racing propulsion, Sensors 23 (2023) 1, p. 58.
DOI: 10.3390/s23010058

[6] A. R. Lewis, E. J. Phillips, W. S. P. Robertson, P. N. Grimshaw, M. Portus, J. Winter, A practical assessment of wheelchair racing performance kinetics using accelerometers, Sports Biomechanics 20 (2021), pp. 1001–1014.
DOI: 10.1080/14763141.2019.1634136

[7] Y. Tai Wang, D. Beale, M. Moeizadeh, An electronic device to measure drive and recovery phases during wheelchair propulsion: a technical note, Journal of Rehabilitation Research and development 33 (1996), pp. 305–310.

[8] Y. Vanlandewijck, D. Theisen, D. Daly, Wheelchair propulsion biomechanics: implications for wheelchair sports, Sports medicine 31 (2001), pp. 339–367.
DOI: 10.2165/00007256-200131050-00005

[9] K. Wong, M. Jaffa, A. Susanto, F. Fuss, Performance analysis in wheelchair racing, in The Impact of Technology on Sport II, Taylor & Francis, (2008).
DOI: 10.1201/9781439828427.ch116

[10] A. D. Moss, N. E. Fowler, V. L. Goosey-Tolfrey, The intra-push velocity profile of the over-ground racing wheelchair sprint start, Journal of biomechanics 38 (2005), pp. 15–22.
DOI: 10.1016/j.jbiomech.2004.03.022

[11] E. Ferlinghetti, J. Braaksma, T. Rietveld, H. Houdijk, R. Vegter, M. Lancini, Comparing marker-less vision systems for contact detection in wheelchair propulsion: evaluating the limitations of angular speed difference, Acta IMEKO 14 (2025) 2, pp. .
DOI: 10.21014/actaimeko.v14i2.2075

[12] T. M. Barbosa, E. Coelho, Monitoring the biomechanics of a wheelchair sprinter racing the 100 m final at the 2016 paralympic games, European Journal of Physics 38 (2017), pp. 044001.
DOI: 10.1088/1361-6404/aa6905

[13] J. G. Richards, The measurement of human motion: A comparison of commercially available systems, Human Movement Science, 18 (1999) 5, pp. 589–602.
DOI: 10.1016/S0167-9457(99)00023-8

[14] World Para Athletics, WPA classification rules and regulations_2023, (2023).

[15] B. S. Mason, J. M. Rhodes, V. L. Goosey-Tolfrey, Validity and reliability of an inertial sensor for wheelchair court sports performance, Journal of Applied Biomechanics 30 (2014), pp. 326–331.
DOI: 10.1123/jab.2013-0148

[16] B. Yu, D. Gabriel, L. Noble, K. N. An, Estimate of the optimum cutoff frequency for the butterworth low-pass digital filter, Journal of Applied Biomechanics, 15 (1999) 3, pp. 318–329.
DOI: 10.1123/jab.15.3.318